OPTIMIZATION OF A NEW MULTI-PURPOSE UAS FOR SCIENTIFIC APPLICATIONS USING AERODYNAMIC RECONFIGURATION

Andreas Scholtz, Karl Kufieta, Peter Vörsmann
Technische Universität Braunschweig, Institute of Aerospace Systems
a.scholtz@tu-braunschweig.de; karl.kufieta@tu-braunschweig.de;
p.voersmann@tu-braunschweig.de

Keywords: *Carolo P 360, Unmanned Aerial System (UAS), Reconfiguration, Autopilot, Real-Time Linux*

Abstract

Unmanned aircraft systems (UAS) have recently become more important, especially for scientific and commercial applications. The field of airborne geosciences has accelerated the demand for a wide range of possible UAS payloads for aerial photography, air chemistry and meteorology. In order to provide a solution to deploy this range of payloads, the Institute of Aerospace Systems (ILR) has developed a new multi-purpose UAS. Therefore a new autopilot system is being developed. This new system is based on the MINC autopilot, which has been used in various field campaigns for aerial photography and atmospheric research. Additional to this, the first completed stage of the new UAS is marked by a new airframe, the Carolo P 360. Due to permanent increasing requirements of operation range and endurance, the efficiency of the UAS should be as good as possible. The here presented approach deals with the reconfiguration of the aerodynamic layout in flight.

1 Introduction

An example for scientific applications with UASs is the project iNTeg-Risk. The intention of this project is the development of an integrated system for fast and automated thread detection in the field of pipeline observations. For this purpose, a digital camera with high resolution and later on an infrared camera shall be implemented into a small unmanned aerial vehicle.

Using such a system for regular observations oil and gas companies will be enabled to obtain a fast overview of the area of a pipeline alignment. An essential part for the realization of this system is the automated flying UAS for which a highly integrated and precise autopilot system is necessary. Due to this task new autopilot hardware with increased processing power will be developed. This includes sophisticated navigation algorithms and the data fusion of the GPS and the inertial measurement unit (IMU). With this solution it is possible to generate georeferenced mosaic images of large observation areas.

The combination of a high resolution digital camera and an infrared camera exceeds the payload limit of all existing UAVs of the Carolo family of the Technische Universität Braunschweig. For this reason a new type of aircraft, the Carolo P 360, is developed. It shall provide increased payload capacity and allow for simplified integration of additional subsystems and sensor packages, such as an emergency landing system [1], while having the same or better endurance and flight performance. To achieve this task a new layout and an optimized aerodynamic design is required. The preliminary results of the aerodynamic reconfiguration system, which were investigated during the first flight experiments, are presented and discussed here as well.

2 Integrated Navigation

2.1 System Architecture

The dimensional limitations on-board a small UAV require the use of sensors based on microelectromechanical systems (MEMS). These are used for the whole Carolo family. The low-cost acceleration and gyroscopic sensors operate at a frequency of 100 Hz but suffer from highly drifting signals. For the compensation of this disadvantage, long-term stable measurements of a single-frequency (L1) receiver for the Global Positioning System (GPS) are used. In this way position, velocity and attitude can be determined at the rate of the inertial measurement unit (IMU) with a better precision than with a stand-alone GPS receiver.

Different concepts for the fusion of sensor data as from GPS and IMU measurements exist [2]. The simplest and therefore most common integration is the so called loose coupling. These systems use the position and velocity information of the GPS to aid the IMU measurements. This approach has the problem that the GPS aiding fails as soon as signals from less than four GPS satellites, which are necessary for a GPS-only navigation solution, are received.

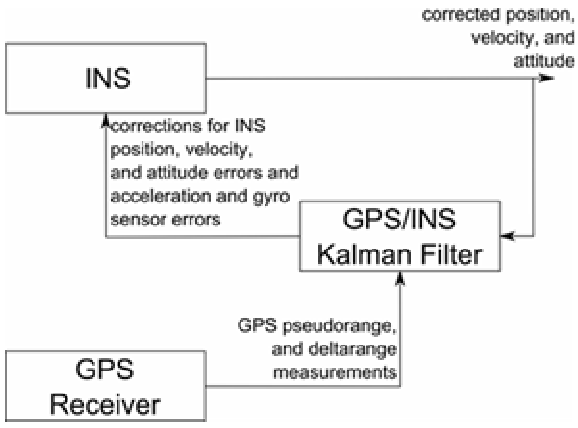

Fig. 1. Tightly Coupled Closed-Loop System [3]

Tight coupling avoids this problem by fusing GPS raw data with IMU measurements. This means, that measurements for pseudo range, delta range, and also carrier phase are used directly in the aiding process. In this way even measurements from one or two satellites have a positive effect on the quality of the navigation solution. On this account a tightly coupled closed-loop system is used for the sensor data fusion. Closed-loop means that the corrected navigation solution from the INS is fed back to the navigation filter to correct the GPS measurements and that the data from the navigation filter is used to correct acceleration and gyroscopic sensor errors (see Fig. 1).

2.2 Navigation Hardware

The Carolo type aircraft are equipped with the Miniature Integrated Navigation and Control System (MINC), see Fig. 2. The MINC board incorporates a MEMS inertial measurement unit, sensors for static and total pressure, a GPS receiver and the on-board computer with the dimensions 80 x 40 x 15 mm³. The total mass including an external GPS antenna is 45 g. The measurement block, which is called TrIMU (left part of Fig. 2), is fully equipped with three orthogonal angular rate sensors and two dual axis acceleration sensors covering the *x*-axis twice with different sensitivities.

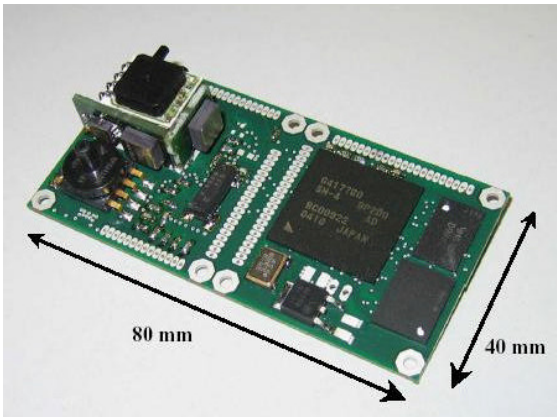

Fig. 2. MINC Autopilot System

2.3 Navigation Filter

The so called Kalman filter, introduced in [4], has become a quasi-standard for accomplishing the data fusion of inertial and satellite navigation. The MINC system is based on a time discrete, linear, closed-loop, tightly coupled error state Kalman filter, see [5]. The error state architecture allows the estimation of a non-linear process with a linear Kalman filter.

The utilized state vector consists of 17 states for errors in position, velocity, attitude, gyro bias, accelerometer bias, and GPS receiver clock error drift.

The Kalman filter works in two phases - prediction and correction. The prediction is executed at the IMU's measurement frequency of 100 Hz. Parallel to the prediction process, the navigation solution is calculated using the IMU measurements. These are processed via a so-called strap-down algorithm, which allows the computation of navigation data from body-fixed inertial sensors, see [6].

The correction process is started when new GPS measurements have arrived. During this update, the received measurements are processed. The filter uses measured values of pseudo ranges, delta ranges, and time differenced carrier phase corresponding to the number of received satellites. The use of the time differenced carrier phase instead of the carrier phase measurement has the advantage, that it is not necessary to solve the phase ambiguity, see [7].

For the post-processing of e.g. during flight recorded image or meteorological data it is crucial to have reliable and accurate data of position and attitude available. On-board the aircraft the above mentioned Kalman filter is used for the sensor data fusion of INS and GPS. At each time step the information from all previous measurements is utilized to generate a precise navigation solution. During the post-processing subsequent to the flight measurement data from before and after the gathering of each measurement is available. Thus, during the post-processing it is possible to use information from previous and future measurements for the sensor data fusion and generation of navigation data. For this purpose a so called Rauch-Tung-Striebel (RTS) smoother is used, see [8].

Besides the increase in precision the application of the smoother has several advantages. The effect of the transient oscillation, which can be observed during the beginning of a linear Kalman filter operation, can be reduced due to the use of future data. Additionally it is possible to bridge GPS outages for a certain amount of time during the post-processing.

2.4 Navigation System Performance

In order to determine the accuracy of the navigation algorithm flight experiments have been done using an IMU with fiber optical gyros (type iMAR iVRU-FC) as a reference. The results of the attitude determination are shown in Tab. 1 with a 1-σ-accuracy. It can be seen that it is possible to calculate a navigation solution of sufficient accuracy using the MEMS based IMU of the MINC autopilot system. Furthermore the results show a significant increase in accuracy due to the use of the RTS smoother.

	lin. Kalman filter	RTS smoother
roll angle	0.4 °	0.3 °
pitch angle	0.4 °	0.3 °
yaw angle	0.9 °	0.5 °

Tab. 1. 1-σ-Accuracy of the Attitude Reference System

3 New Autopilot System

The ILR has developed a new autopilot system to overcome the emerging computing requirements for complex algorithms like dynamic inversion or navigation filters. The system consists of a Main Computing Unit (MCU) and the Main Sensor Unit (MSU) which can be expanded with numerous Mini Satellite Endpoints (MSE). The principal components, MCU and MSU are tightly connected to form a system with a size of 40 x 70 x 15 mm³, weighting around 50 g including an optional Wi-Fi antenna or 40 g without Wi-Fi. The system offers 10 Servo channels, two USB-Ports, CAN-Bus, GPS and telemetry connections. The power consumption is between 1 Watt to 2 Watts depending on the processor clock rate and an additional 0.5 Watts for Wi-Fi.

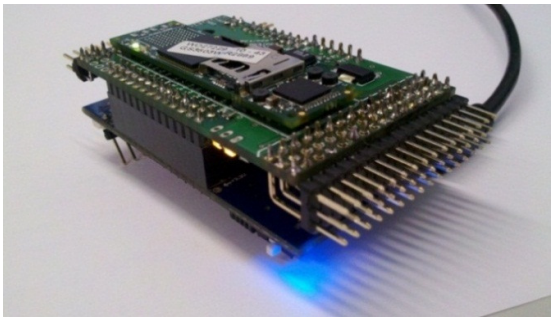

Fig. 3. The New Autopilot System

3.1 Main Computing Unit

The MCU contains two processors: a small STM32 processor handles data acquisition and provides the CAN bus interface to remote satellite endpoints. The second processor, an OMAP3530 offers 720 MHz of computing power for complex control and navigation algorithms or even for image processing. The Real-Time Linux operating system offers multi-threading and a guaranteed execution time for real-time threads. At the same time it is possible to use high level drivers and libraries for LAN or USB. The real-time capability of the operating system is determined by an upper bounded delay in the thread execution as depicted in Figure 4. It is visible that the average latency is between 20 µs and 40 µs depending on the load from other threads but that the real-time thread is executed within 62 µs.

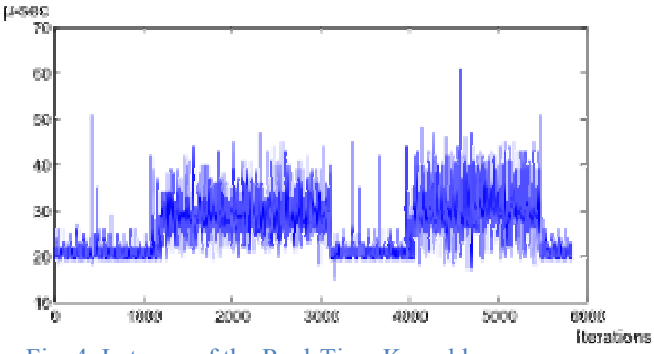

Fig. 4. Latency of the Real-Time Kernel has an upper bound of 62 µs

3.2 Satellite Endpoints

Tiny (30 x 30 mm²) extension modules are connected via CAN-Bus to the MCU and can be placed anywhere in the aircraft. The satellite modules offer additional servo and A/D ports for sensors as seen in Fig. 5.

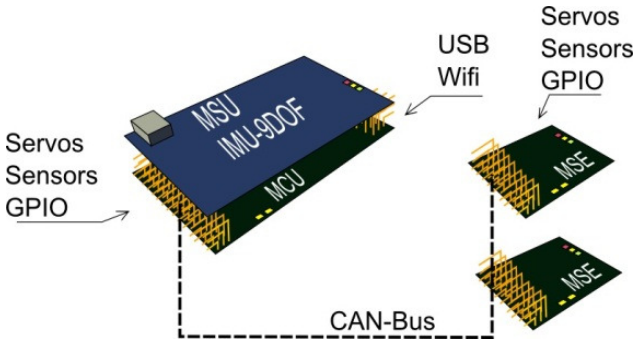

Fig. 5. Schematic of the System with MSU, MCU and Satellite Endpoints

3.3 Programming

All interfaces and all processors are programmed via the Simulink Real-Time Workshop with a 'one mouse click' solution. Required hardware interfaces e.g. a sensor is modeled in a Simulink block which can be moved via drag-and-drop from the library to the model. Figure 6 shows a simple program for the processor with the hardware blocks for LED's, Servos and CAN-Signals. Additionally it is possible to use the so called external mode on the OMAP3530 processor via Wi-Fi. This allows monitoring the hardware and setting of the hardware parameters directly from the development environment in the development model. It is expected that research and development cycles can be reduced by these techniques.

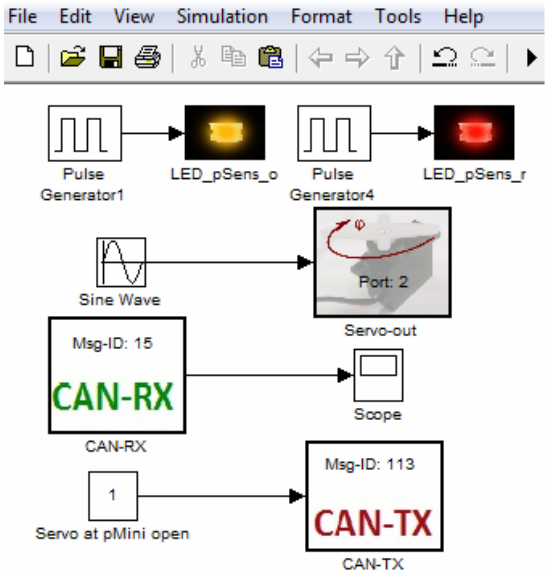

Fig. 6. A Simple Test Program of the MCU

3.4 Multitasking Process in Linux

The Kalman filter is implemented in m-Files in Mathworks Simulink. After the execution of the autocode build process, the created program is started. The program itself starts different threads, corresponding to the different clock frequencies in the Simulink Model. The strap-down part of the Kalman filter is calculated in a 100 Hz thread as a process with priority 98 and needs 5.4 ms calculation time. Additionally the estimation process is started by a GPS triggered thread with the priority 96 (see Fig. 7). It would

not be possible to run the estimator without multitasking in the 100 Hz thread because the estimator requires more than 10 ms time. The following diagram shows the segmentation of the threads.

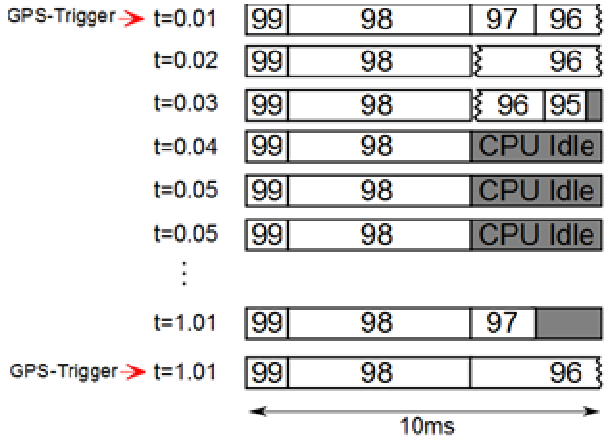

Fig. 7. Thread Execution Order on the Real-Time Operating System

The numbers 95 to 99 represent threads where 99 is the highest thread priority. Table 2 shows the different threads and the measured execution times on the real-time operating system. The UART and the SPI threads correspond to hardware drivers called in the 100 Hz thread, thus they must be executed with a higher priority.

Priority	Thread	time
99	UART SPI	100 µs 823 µs
98	100 Hz thread	5.4 ms
97	10 Hz thread	1 ms
96	GPS triggered	10.2 ms
95	1 Hz thread	1 ms

Tab. 2. Execution Times on the OMAP3530 Hardware

As shown in the thread delay and thread execution time it is possible to run complex algorithms from C-code from Simulink models on the Real-Time Linux to operate an autopilot system.

4 The New Airframe Carolo P 360

4.1 Current Aircraft

Since 2001, micro and mini unmanned aircraft are developed at the ILR. The latest aircraft type of the Carolo family is the single-engined Carolo P 200 (Fig. 8) and the twin-engined Carolo T 200 with a wingspan of 2 m and a maximum take-off weight of 7 kg including 1.5 kg of payload.

Fig. 8. Carolo P 200

The maximum endurance is more than one hour at a cruising speed of 22 m/s. These UASs are typically used for remote sensing applications [9] and for meteorological measurements in meteorological mini aerial vehicle (M²AV) configuration [10].

4.2 Aircraft Concept

The all new Carolo P 360 further increases the payload limit and enhances the handling on the ground. Due to its modular design a convenient pack size and transportability are achieved. The system is fast reassembled with a minimum of required tools. The P 360 is able to carry an emergency landing system and an adaptive jettisonable undercarriage. The main technical design restrictions are listed in Table 3.

parameter	**value**
maximum take-off weight	25 kg
maximum payload mass	2.5 kg
operation temperature	-20°C to +45°C
transport size	longest part < 1.6 m
endurance	electric 45 min, combustion 2 h
cruising speed	20 - 30 m/s
maximum wind speed	15 m/s
maximum assembly time	15 minutes

Tab. 3. Design Restrictions of the Carolo P 360 [1]

The restriction to a smaller transport size compared to the Carolo P 200 makes a modular aircraft concept necessary. The UAV should be able to transport a meteorological sensor package for turbulence and wind measurements. For this payload, a free airflow from the front is required, which leads to a twin engine or a pusher configuration. A single engine solution is preferred, because of the higher efficiency. The resulting design is a conventional aircraft with a centre payload and engine part, a wing with a moderate aspect ratio and two tailbooms with standard tail (Fig. 9).

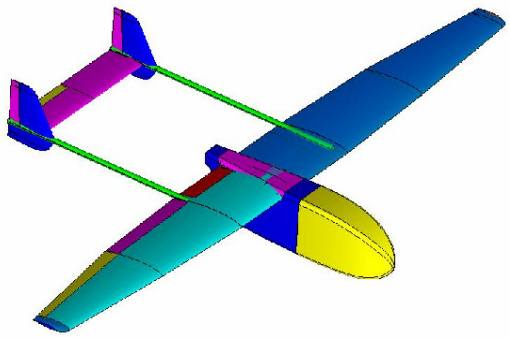

Fig. 9. Concept of the new Carolo P 360

An additional requirement is the fast and easy exchange of the payload. This is especially important for the use under ever changing requirements in the academic domain.

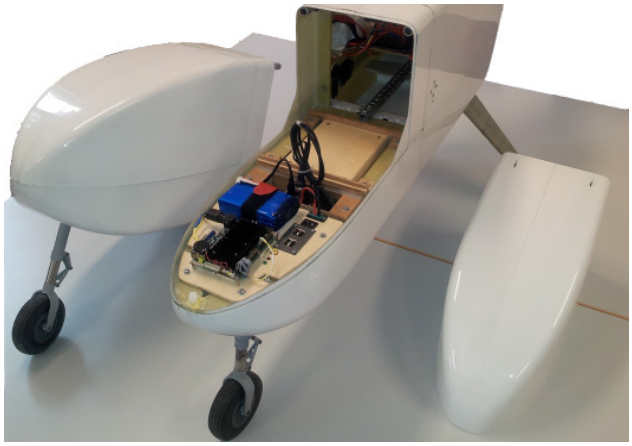

Fig. 10. Modular Payload Bay

Therefore a modular payload bay is developed. The whole fuselage front is removable and can be exchanged within few minutes. This also could be interesting for other customers who like to design their own payload bay. Just the mounting points, the delivered connector for energy and communication with the autopilot system and the moment around this frame to keep the centre of gravity are defined. Figure 10 shows modular payload bays (mounted and unmounted) including the hood, which covers the service entry for accumulator exchange and payload integration.

4.3 Aerodynamic Layout

The most widely used meteorological sensor package is calibrated for an airspeed of 22 m/s. For this reason, this is the design velocity of the Carolo P 360. From the beginning of this project it was planned to design an aircraft with the possibility to optimize the aerodynamic wing configuration for all existing values of the lift coefficient C_L. The wing is therefore equipped with three flaps for each side. That way, it is possible by adjusting the camber distribution for every speed close to the optimal elliptic circulation distribution. The reason for this is that the drag coefficient C_D (Eqn. 1) is minimized, which is influenced by the minimum drag coefficient C_{D0}, the induced drag coefficient C_{DI}, the trim depended drag C_{DTrim} and the parasite drag coefficient C_{DP}.

$$C_D = C_{D0} + C_{DI} + C_{DTrim} + C_{DP} \qquad (1)$$

The wing shape is designed to achieve this optimum. It results in a minimum induced drag coefficient caused by an Oswald efficiency e close to 1 (Eqn. 2). The Oswald efficiency can reach values between $0 < e \leq 1$. The aspect ratio AR is a design parameter and depends on the maximum wing span and the required wing area.

$$C_{DI} = \frac{1}{e \cdot \pi \cdot AR} \cdot C_L^2 \qquad (2)$$

An additional advantage of the flaps is their dual use as striking airbrake, which reduces the required size of the landing field. The

local lift coefficient distribution is also very important because it gives an impression of the aircrafts handling. Therefore the local lift coefficient which is predominantly influenced by the wing shape and the airfoil loft should be nearly constant in the centre wing area and decrease smoothly towards the wing tip. With such a distribution the UAV is still controllable at stalling conditions. Figure 9 shows the diagram for the design velocity and an aircraft weight of 22 kg. Therein it is perceivable, that the local lift coefficient homogenously disturbed along the inner wing area. The curve decreases at the outer 20 % of the wingspan only. This indicates a docile stall behavior.

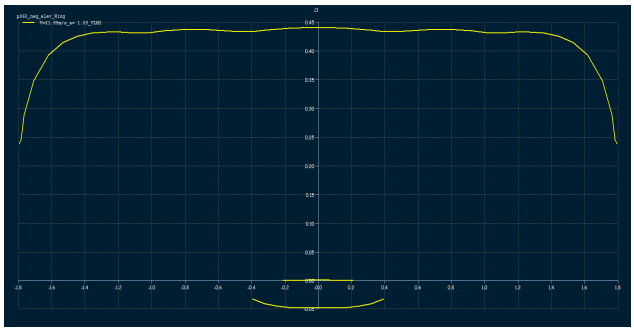

Fig. 11. Distribution of Local Lift Coefficient with XFLR5 [11]

The choice of the airfoil loft is also very important to increase the flight performance. The airfoils must fulfill different tasks. They have to work efficiently with flaps, provide a very high maximum lift coefficient and a smooth stalling behavior. The airfoil family HQ-W fits these constraints very well and is chosen for the new Carolo P 360 [1]. The combination of this airfoil loft and the accurate wing shape design delivers a maximum simulated glide ratio of 32 for a trimmed configuration at a velocity of 25 m/s. In this simulation only the aerodynamic surfaces were used because the simulation of the stream around a 3D body like the fuselage is not proven. In first flight experiments with a model of the new airframe in half size a stationary decent is performed, see [12]. The resulting glide ratio during this flight is calculated to 12.5, which is much lower than the theoretical value. The reason for this is the additional drag of the fuselage including propulsion system, the tailbooms and the interference drag between all parts. Typical values for this type of aircraft are between 10 and 12, so that this result represents a good aerodynamic efficiency for the new Carolo P 360 model.

4.4 Flight Experiments

The following flight experiments are flown with a full scale airframe, as depicted in Figure 12, to measure the glide ratio and its change by using different camber distributions. The goal is to increase the glide ratio over a wider range of airspeeds and reduce so the energy consumption. Therefore several descent flights with alternating flap positions and velocities are performed.

Fig. 12. Full Scale Carolo P 360

4.4.1 Simulation Results

The in chapter 4.3 introduced simulation software is used to generate the glide ratio polar for three different flap positions (5°, 0° and -5°) and the full range of cruising speeds.

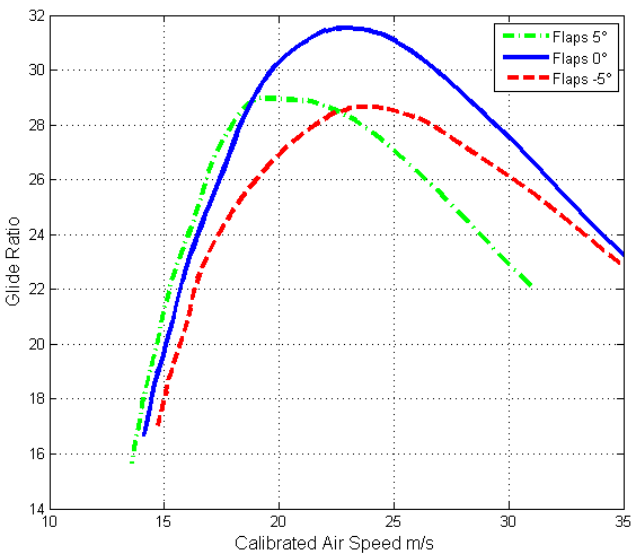

Fig. 13. Simulated Glide Ratio Polar

The aircraft had the same take-off weight of 18.4 kg but only the aerodynamic surfaces without fuselage and landing gears are simulated. The results are shown in Figure 13. For slow airspeeds the glide ratio of the wing with positive flap deflection shows a higher value (dash-dotted line). The same trend was expected from the negative flap deflection (dashed line), but in this diagram the neutral position of the flaps (solid line) shows the best results, also for fast cruising speeds. A reason for this could be the missing interference of the aerodynamic surfaces with the missing parts of the aircraft.

4.4.2 Experimental Setup

For this preliminary investigation all control surfaces over the wing span, including the ailerons, had the same angle. The recommended flap angles are +4°, 0° and -4°. They are given by the airfoil designer [13]. The experiments are flown with constant velocities between 16 m/s and 32 m/s to cover the full range of cruising speeds, see Table 3. During this experiment the aircraft had a take-off weight of 18.4 kg. The navigation hardware MINC, which is presented in chapter 2, including the filter software is used as measurement unit for these experiments. Additional to the barometric and electro-mechanic sensors the commanded PWM-signals for the servos are logged to ensure, that the flaps were in the predefined position. The weather condition was constant but not ideal for all flights. The wind was relatively strong and steady with about 8 m/s in eastern direction and some weak convective wind components. Therefore the measurement flights are performed against the wind and for a long period to minimize the influence of horizontal and vertical gusts.

4.4.4 Analysis

As an example of the raw data the measurement plots for barometric height (Fig. 14) and calibrated airspeed (Fig. 15) over time are given for the experimental flight with a negative flap deflection of -4°. For each flap position nine descent flights are performed in the given velocity range with increments of 2 m/s.

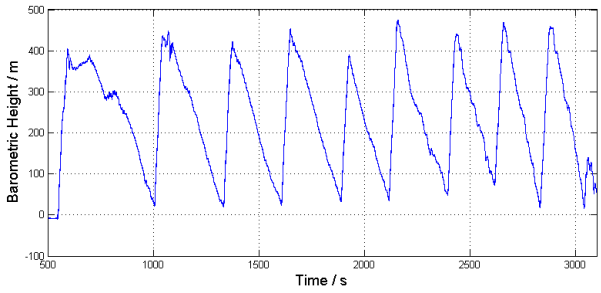

Fig. 14. Measuring Plot of the Barometric Height over Time

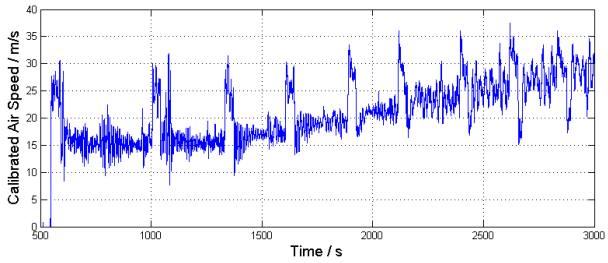

Fig. 15. Measuring Plot of the Calibrated Airspeed over Time

Due to the fact, that only the dynamic and static pressure could be used for the flight performance measurements, some simplifying assumptions are made. The experiment was set up for symmetrical flight conditions and a stationary descent flight. So the calibrated airspeed is defined as

$$V_A = \begin{pmatrix} u \\ v \\ w \end{pmatrix} \tag{3}$$

with the horizontal speed component v = 0 m/s. For each descent flight a linear regression has to be calculated for the height over time.

$$H = \dot{H} \cdot t + H_0 \tag{4}$$

Therein the searched descent rate w is given to:

$$w = -\dot{H} \tag{5}$$

The calibrated airspeed has to be analyzed in the same way. The linear regression leads to the following function.

$$V_A = \dot{V}_A \cdot t + V_0 \tag{6}$$

With

$$\dot{V}_A \approx 0 m/s \tag{7}$$

the constant average airspeed for each descent could be calculated with

$$t = t_1 + \frac{t_2 - t_1}{2} \qquad (8)$$

wherein t_1 and t_2 are defined as the beginning and end of each measurement section. With the definition of the airspeed components shown in Figure 16, the horizontal airspeed u could be calculated.

$$u = \sqrt{V_A^{\,2} - w^2} \qquad (9)$$

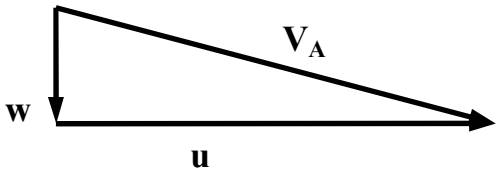

Fig. 16. Definition of Airspeed Components

With the now known horizontal and vertical airspeed components it is possible to generate a velocity polar by plotting the parameter pairs in a diagram. This point cloud is analyzed by a cubic regression function. By using the resulting function the glide ratio polar could be generated with the definition of the reciprocal glide number

$$\varepsilon = -\tan\gamma = \frac{w}{u} \qquad (2)$$

and the glide number:

$$E = \frac{1}{\varepsilon} \qquad (3)$$

The resulting glide ratio polar for the three experimental setups are given in Figure 17. Herein the maximum glide ration is 15.3, which is about the half of the simulated value. The reason for this is the influence of the additional drag produced by e.g. the fuselage. Compared to the results of the half scale model, the glide ratio is much better. One reason for this may be the higher Reynolds number and with this the less critical conditions on the airfoils. There is much clearer separation of the maximum for each glide ratio compared to the simulated polar. This separation over the airspeed was expected whether the absolute maximum value was expected for the neutral flap deflection (solid line). The higher glide ratio for the positive deflected flaps (dash-dotted line) may be a result of the weather condition.

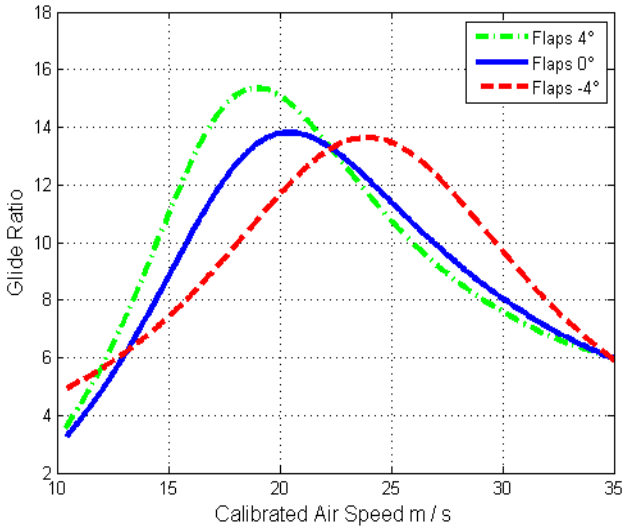

Fig. 17. Experimental Glide Ratio Polar

The polar distribution over the calibrated airspeed shows, that the maximum cruising speed of 30 m/s is for this setup very inefficient while the design speed, represented by the maximum glide ratio of the not deflected flap position, is here at about 20.5 m/s. This is caused by a relatively light take-off weight, which normally is 22 kg. The benefit of the reconfiguration for this experiment is an increased glide ratio of 43% at an airspeed of 16.8 m/s and 24% at 26.9 m/s which are enormous winnings.

5 Conclusion and Outlook

The all new aircraft Carolo P 360 had to be developed to increase the payload and flight performance to a new level. This UAV is equipped with the MINC autopilot system. In the near future, the new autopilot system presented in section 3 will be implemented to increase the processing power, which makes it possible to geo-reference the payload information in flight and to offer new functions like an automatic optimized aerodynamic setup. This leads to an UAV with convenient handling characteristics and an increased efficiency. The promising looking results of the flight experiments should be investigated with some more detailed ex-

periments including a wind speed compensation to minimize this influence. This shall be done by implementing a meteorological sensor package and flying at better wind conditions.

Acknowledgments

Project iNTeg-Risk is funded by the European Union in the Seventh Framework Programme under Grant Agreement CP-IP 213345-2. Additional to this I like to thank my colleagues C.-S. Wilkens, C. Kaschwich and G. Scholz for their support during the flight experiments and data analysis.

References

[1] Scholtz A. *Design and construction of a UAV-prototype with emergency landing system.* Diploma Thesis F 0828 D, Institute of Aerospace Systems, TU Braunschweig, 2009.

[2] Farrell J L, Barth M. *The Global Positioning System and Inertial Navigation*. McGraw-Hill, New York, USA, 1999.

[3] NAVSTAR GPS. *User equipment introduction*. United States Coast Guard Navigation Center, www.navcen.uscg.gov/pubs/gps/gpsuser/gpsuser.pdf , 2011.

[4] Kálmán R E. A new approach to linear filtering and prediction problems. *Transaction of SME – Journal of Basic Engineering,* 82(2), pp. 35-45, 1960.

[5] Winkler S, Vörsmann P. Multi-sensor data fusion for small autonomous unmanned aircraft. *European Journal of Navigation,* 5(2), pp. 32-41, 2007.

[6] Kayton M, Fried W R. *Avionics navigation systems*. 2nd edition, John Wiley & Sons, Inc., New York, USA, 1997.

[7] Farrell J L. Carrier phase processing without integers. *Proceedings of Institute of Navigation 57th Annual Meeting/CIGTF 20th Biennial Guidance Test Symposium,* Albuquerque, New Mexico, USA, pp. 423-428, 2001.

[8] Rauch H E, Tung F, Striebel C T. Maximum likelihood estimates of linear dynamic systems. *AIAA Journal,* 3(8), pp. 1445-1450, 1965.

[9] Krüger T, Wilkens C-S, Reinhold M, Selsam P, Böhm B, Vörsmann P. Ergebnisse des ANDROMEDA-Projektes - Automatische Luftbildgewinnung mit Unbemannten Kleinflugzeugen. *Deutscher Luft- und Raumfahrtkongress*, Paper ID 161314, 2010.

[10] van den Kroonenberg A, Martin T, Buschmann M, Bange J, Vörsmann P. Measuring the wind vector using the autonomous mini aerial vehicle M2AV. *Journal of Atmospheric and Oceanic Technology*, American Meteorological Society, 2008.

[11] Drela M, Youngren H. *XFLR5 Aerodynamic layout program*. Massachusetts Institute of Technology, USA, http://xflr5.sourceforge.net/xflr5.htm, 2008.

[12] Scholtz A, Krüger T, Wilkens C-S, Krüger T, Hiraki K, Vörsmann P. Scientific application and design of small unmanned aircraft systems, *14th Australian International Aerospace Congress*, Melbourne, Australia, paper no. 58.00, 2011.

[13] Quabeck H. *Profilsammlung HQ-W-Serie.* HQ Modellflugliteratur, http://www.hq-modellflug.de/Koordinatenframe.htm, 2011.

Copyright Statement